



RESEARCH ARTICLE



Fe-Al intermetallic suppression of dissimilar RSW joints using stainless-steel interlayers

Bryan Lara^a, Rafael Giorjao^a, Hassan Ghassemi-Armaki^b and Antonio Ramirez oa

^aWelding Engineering, The Ohio State University, Columbus, OH, USA; ^bGeneral Motors R&D, Manufacturing Systems Research Laboratory, MI, USA

ABSTRACT

Austenitic and ferritic stainless-steel interlayers for resistance spot welding of an AlSi-coated 2000MPa UTS press-hardened boron steel and a 6022-T4 aluminium alloy were investigated to improve joint performance. CALPHAD and kinetic-based simulations were explored to determine the effects of Cr on the formation of Fe–Al intermetallic compounds. Selected area diffraction reveals the formation of FeCrAl9 along the interlayer-Al interface and suppresses the formation of FeAl3. The implementation of stainless-steel interlayers significantly improved the mechanical performance of the joint, with the 430 foil condition experiencing a substantial decrease in the Fe–Al intermetallic.

ARTICLE HISTORY

Received 13 July 2022 Revised 10 January 2023 Accepted 29 January 2023

KEYWORDS

Usibor 2000; 6022-T4; Fe-Al interface; CALPHAD; DICTRA; chromium; stainless steel; transmission electron microscopy; finite element modelling

Introduction

Interest in joining technologies for multi-metallic hybrid structures has increased for decades. Multi-materials designs with steels and light metals, such as aluminium alloys, are being extensively pursued to address the increasing demand for vehicle light-weighting. Low-density alloys such as aluminium introduce weight savings. At the same time, the implementation of advanced high-strength steels with their high alloying additions makes them desirable for their strength and ductility [1,2]. Nevertheless, implementing different material combinations, such as forming brittle intermetallic compounds, brings challenges.

Intermetallic phase formation at elevated temperatures depends on the chemical potential difference, mobilities of the constituent elements, and the nucleation conditions at the beginning of welding [3]. Owing to iron's low solubility in aluminium, a brittle intermetallic compound layer can form at the fusion weld interface. The intermetallic compound layer results from a reaction between Al and Fe and serves as the bond between the two materials [4,5]. If not well controlled (distribution and morphology), it deteriorates the weld's load-bearing capacity due to the brittle nature of the intermetallic layer [6,7]. During Al-Steel joining, the appearance of FeAl₃ and Fe₂Al₅ are of great importance as they hinder welded joints' mechanical performance [8]. Notably, the intermetallic compounds FeAl₃ and Fe₂Al₅ exhibit parabolic growth behaviour influenced by both time and temperature [9].

Magnetic-assisted and metallic bump-assisted RSW have been explored to reduce the IMC layer thickness [10,11]. However, using metallic interlayers, which act as barriers between Al-Fe, also shows promise because they inhibit the intermetallic compounds' growth kinetics. In previous work involving Al-Fe joining with interlayers, it was determined that as interlayer thickness increased, the intermetallic layer decreased [12-15]. Besides this, little is known about interlayer composition effects on the intermetallic layer and mechanical performance. Interlayer materials containing elements such as Al, Zn, and Si have been implemented in research; however, one key element that has limited exposure in literature and has been shown to mitigate the formation of the intermetallic layer is chromium. Cr has a significant effect on lowering the interdiffusion between FeAl₃ and Fe₂Al₅. As the Cr content increases, the layer thickness of FeAl₃ remains constant while the Fe₂Al₅ layer thickness experiences a significant reduction [16-18]. Besides this, forming Al_x(Fe,Cr)_x intermetallic phases decreases the diffusion interaction between the Fe and Al interface. Thus, this work explores a fundamental approach to the Cr effects on the Fe-Al system not seen in dissimilar resistance spot welds and differs from previous work conducted [15].

The present study explores the influence of a stainless-steel interlayer on the Fe-Al intermetallic. The tensile shear performance of a resistance spot welded aluminium alloy and press-hardened boron steel are also compared among the interlayer conditions.

Table 1. Nominal chemical composition of PHS, aluminium, and interlayers in wt-%.

Material	C	Si	Mg	Mn	Cr	Ni	Мо	Al	Fe
*PHS	0.36	0.80	-	1.40	0.70	0.35	0.70	_	Bal
AA6022	-	0.80	0.60	0.10	0.30	-	-	Bal	-
Foil 304	0.05	0.20	-	2.00	18.00	8.00	0.40	-	Bal
Foil 430	0.06	0.36	-	0.32	16.37	0.20	0.03	-	Bal

*Maximum composition.

PHS, press-hardened boron steel.

Table 2. Resistance Spot Welding parameters and electrode dimensions.

Al Electrode	F – Type Cu – Zr alloy ø16			
PHS Electrode	B – Type Cu – Zr alloy ø8			
Electrode Force	5.3 kN			
Squeeze Time (ms)	500			
Weld Current (kA)	16-16-16			
Weld Time (ms)	166-166-166			
Cool Time (ms)	30-30			
Hold Time (ms)	240			

Materials and experimental procedure

The materials used in this study involved a 2.0 mm thick 6022-T4 aluminium alloy and a 1.6 mm thick AlSi-coated 2000MPa UTS press-hardened boron steel (PHS) with dimensions of 150 mm \times 50 mm. The interlayers used were in foil form with a thickness of 250 μm . The interlayers consisted of austenitic 304 and ferritic 430-grade stainless steel. Table 1 shows the chemical composition of all the materials used in this study. The chemical composition was obtained using an arc/spark optical emission spectrometry metal analyzer.

The weld schedule, shown in Table 2, was used for each interlayer condition to reduce the testing matrix. The aluminium sheet was placed on the positive electrode to consider the thermoelectrical Peltier effect, resulting in decreased applied heat. Before welding, the aluminium oxide layer was reduced using 240-grit sandpaper. The electrodes used were RWMA Class 1 CuZr electrodes provided by Luvata Corp. The aluminium side electrode consisted of an F-type 16 mm face diameter with a 3 mm radius with the manufacturer designation FF25Z08. The steel side electrode was a dome B-type 8 mm face diameter (FB25Z24). Aluminium and PHS have different thicknesses and thermal conductivities and require asymmetrical electrode caps to avoid heat balance problems which would result. The welding was carried out using a medium frequency direct current RSW machine at room temperature.

The aluminium nugget and intermetallic measurements were obtained through ImageJ software. The intermetallic layer was measured along the centre of the joint starting from the Fe interface. Ten measurements were taken for each condition using a spacing of 0.5 μm accounting for the morphology of the intermetallic layer. Once welded, the samples were pulled in tensile shear configuration per AWS D8.9M using an MTS 810 machine. A total of three tests were performed for

each condition using a quasi-static loading with a displacement rate of 1 mm/min. The fracture energy was obtained from the area under the force/displacement curve at the peak force value; this was done not to include the bending and rotating effects after the peak force value was achieved. All data used a 95% confidence interval for statistical significance.

The welded coupons were cut 0.5 mm from the weld centerline parallel to the loading direction. The samples were cold mounted in the epoxy, ground, and vibratory polished with 0.05 µm colloidal silica. Once polished, the test specimens and intermetallic compound layers were analyzed using an Apreo 2 scanning electron microscope (SEM). A Tecnai F20 transmission electron microscope, in which foils were prepared by focused ion beam lift-out done on a Nova NanoLab 600 DualBeam SEM. For increased accuracy, selected area diffraction was used to determine the intermetallic compounds in conjunction with crystal maker software and the inorganic crystal systems database (ICSD).

Free energy calculations were created using the 2021a version of thermodynamic Thermo-Calc[©] software using the TCFE10 iron and MOBFE6 mobility databases. Chromium concentrations ranging from 1 to 25 wt-% were used to determine the effects of a 60 wt-% Al-Fe matrix on the intermetallic layer, thus varying the iron and chromium concentration. The temperature range used for the simulations was from 700°C to 1100°C. Diffusion-controlled transformation simulations were also conducted for 0.5 s at 950°C using a Fe matrix consisting of different compositions such as 90 wt-% Fe - 10 wt-% Cu, 90 wt-% Fe - 10 wt-% Cr, 90 wt-% Fe - 10 wt-% Si, 90 wt-% Fe - 10 wt-% Ni, and 90 wt-% Fe – 10 wt-% Ti to further showcase the inhibiting effects of Cr on the Fe-Al intermetallic layer.

Results and discussion

CALPHAD and kinetic modelling

The effect of Cr on a Fe matrix was assessed using a free energy diagram for the FeAl₃ intermetallic that was calculated using CALPHAD. Figure 1 shows the free energy of FeAl3 for increasing temperature and Cr concentrations. A lower Gibbs free energy corresponds to a more spontaneous reaction. The surface plot shows a considerable increase in the Gibbs free energy of FeAl₃ between 0 and 25 wt-% Cr as the temperature rises from 700°C to 1100°C. The analysis was

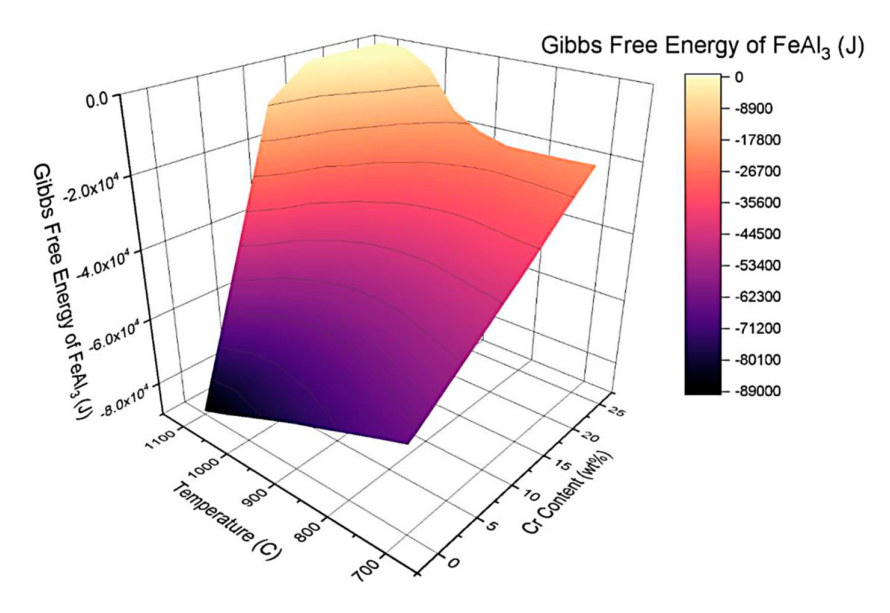


Figure 1. Free energy of FeAl₃ with varying temperature and chromium concentration.

restricted to FeAl₃ as it is the first intermetallic phase to form; thus, by effectively inhibiting the likelihood of precipitating FeAl₃, the suppression, and growth of Fe₂Al₅ can also be influenced. Noticeably, Cr can significantly reduce the formation of FeAl₃. Chromium thus minimises the interaction between Fe and Al, resulting in the precipitation and growth of Fe_xCr_y, Al_z intermetallic compounds. The Fe–Al intermetallic growth is suppressed, illustrated by the higher Gibbs free energy value [19].

Aluminium transport in Fe occurs via crystal lattice defects such as grain boundaries and dislocations. These defects are low energy barriers for nucleation and growth of intermetallic precipitates. The effects of Cr on the diffusion of Al in a Fe matrix were further evaluated and compared with other elements such as Cu, Si, Ni, and Ti seen in Figure 2, the Al diffusion distance is 100 wt-% Fe is large and thus results in a thick intermetallic layer. The introduction of Ni does not suppress the diffusion experienced in the Fe-Al system. Cu and Ti decrease the Al diffusion distance by 0.2 um. The decrease is attributed to the suppression of the FeAl₃ phase, obtained using the CALPHAD software. Noticeably, Cr and Si decrease the Al diffusion distance by 1.0 μm. The suppression of the Al diffusion from Si additions has been attributed to Si atoms occupying vacancies along the c-axis of the Fe₂Al₅ orthorhombic lattice [20–23]. Cr is a larger atom and thus inhibits the Fe-Al differently through the formation of Fe_xCrAl_v compounds [16,17,19].

Mechanical performance

Tensile shear testing revealed a substantial improvement in force and fracture energy of the 6022 – PHS joint through the stainless-steel interlayers, as shown in

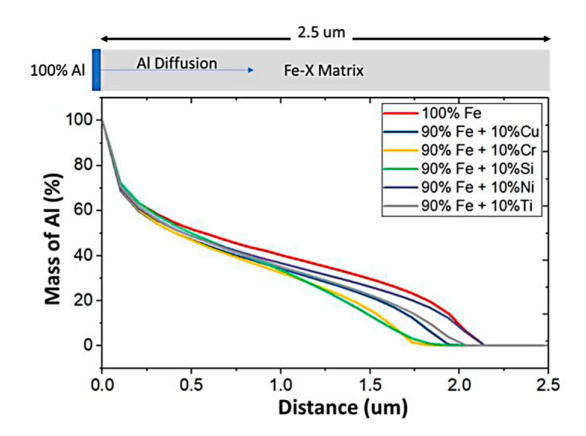


Figure 2. Al diffusion comparison in a Fe-10 wt-% matrix

Figure 3. The 430 foil condition improved the force and fracture energy, which saw an increase of 4.8 kN and 1.5 J compared to the no interlayer sample. The performance gain is credited to a reduction of the Fe–Al intermetallic layer and an increase in the weld nugget diameter. The increased weld nugget diameter results from a higher joule heating effect from the additional contact resistance generated along the interlayer interfaces.

However, each condition exhibited different nugget diameters of 8.5 ± 0.5 , 9.3 ± 0.4 , and 9.2 ± 0.2 for the no interlayer, 304 and 430 foils, respectively. Joint efficiency was used to normalise the data. Figure 4 compares the macrostructure of the no interlayer and foil 304 conditions. As shown in Figure 4(a), the HAZ outline is visible and melting along the dissimilar metal interface and porosity. Figure 4(b) illustrates similar features but with melting between the stainless-steel foil and PHS. The interlayer condition shows more indentation than the no interlayer joint resulting from

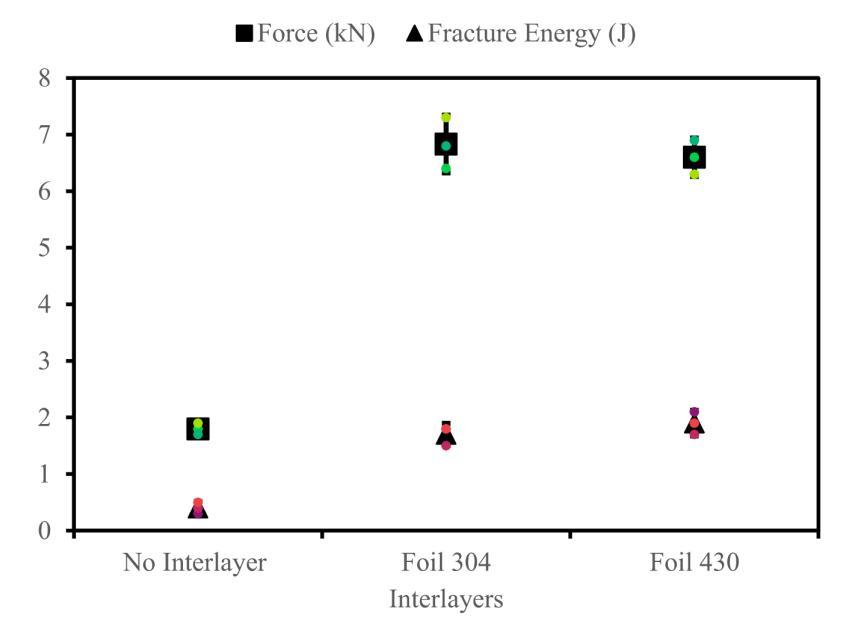


Figure 3. Comparison of tensile shear performance of interlayer joints.

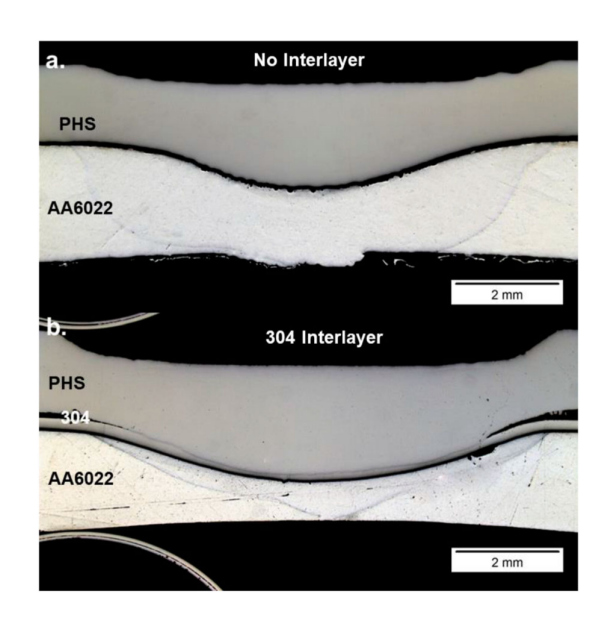


Figure 4. Macrostructure comparison of (a) no interlayer (b) 304 interlayer conditions.

the increased joule heating response. Consequently, a higher degree of deformation is experienced by the interlayer joints.

The nominal peak tensile stress is calculated for an interfacial failure mode as shown in Equations 1. σ_{IF} uses the area of the aluminium nugget (πr^2) because fracture occurs through the sheet-to-sheet interface of the joint [24–26]. For simplicity, the ultimate tensile strength of the aluminium base material was used to determine the joint efficiency of the fracture. It is difficult to quantify the rotating stresses acted upon the joint during tensile shear testing. The joint efficiency for the no interlayer, 304 and 430 foil interlayers, was calculated using Equation (2) and determined to be

15%, 44%, and 45%, correspondingly. All joints failed in the interfacial failure mode due to the large thicknesses of the aluminium and PHS. In the no interlayer condition depicted in Figure 4(a), the joint failed along the AA6022-PHS interface near the IMC layer. The interlayer joints all failed along the AA6022-SS interlayer interface. To inhibit the interfacial failure mode, a thinner sheet of aluminium would lower the aluminium/steel thickness ratio and reduce the shear-totensile ratio, effectively lowering the shear stress at the weld-faying surface [27].

$$\sigma_{IF} = \frac{\text{Peak Force}}{\pi r^2}$$

$$E_W = \frac{\sigma_{IF}}{\text{UTS}_{Al}}$$
(2)

$$E_W = \frac{\sigma_{IF}}{\text{UTS}_{AI}} \tag{2}$$

Intermetallic layer

Figure 5(a) illustrates the compositional gradient present within the Fe-Al intermetallic consisting of two distinct layers, FeAl2 and FeAl3, with a thickness of 1.8 μ m \pm 0.1. The formation of a eutectic grain in Figure 5(b) has been found to be related to an orientation relationship between FeAl and FeAl₂ [28] Figure 5(c) illustrates the diffraction pattern of the FeAl₂ compound, which matched the ICSD reference 260874; FeAl2 is a triclinic crystal. The crystal was observed in the [001] orientation. Energy Disperive Xray Spectroscopy mapping (Figure 5(d)) shows FeAl₂ having a composition of 66.5 at.-% Al - 33.5 at.-% Fe. The lighter area near the aluminium has a composition of 73.6 at.-% Al - 26.4 at.-% Fe thus indicating the FeAl₃ compound. Importantly, Si can be observed within the intermetallic layer, but was found to have roughly 1

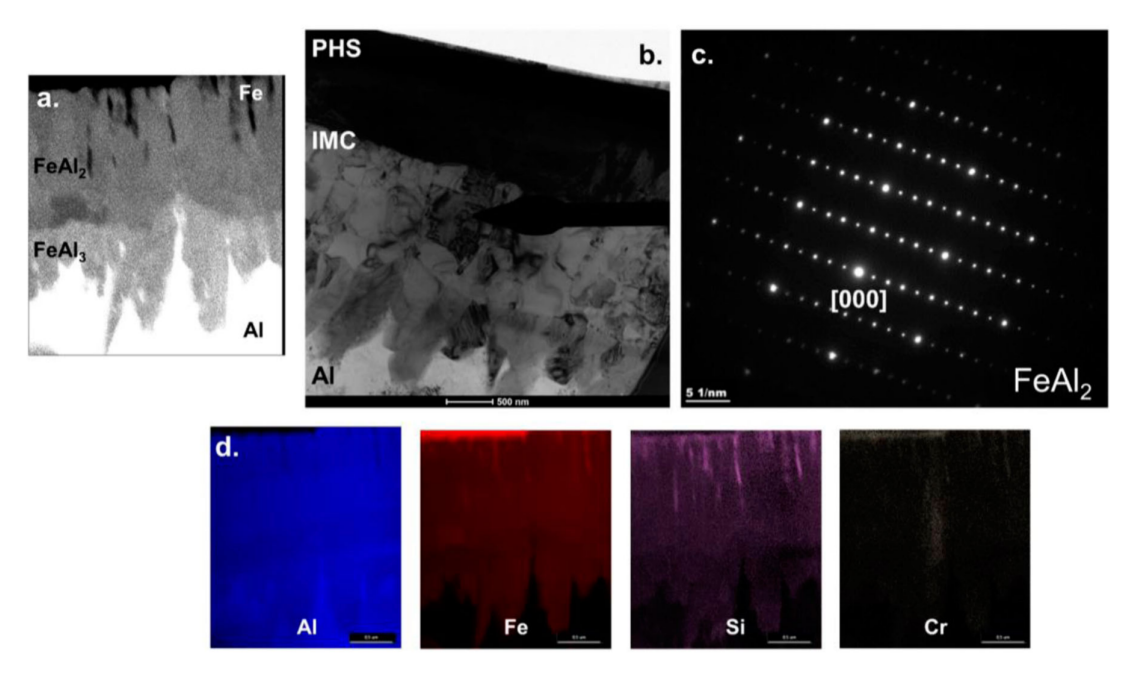


Figure 5. (a) Ratio of Fe and Al using transmission electron microscope (TEM) EDS maps from images in (d); (b) BF TEM images; (c) selected area diffraction (SAD) of grain next to the beam stopper; (d) TEM EDS mapping of image in (a).

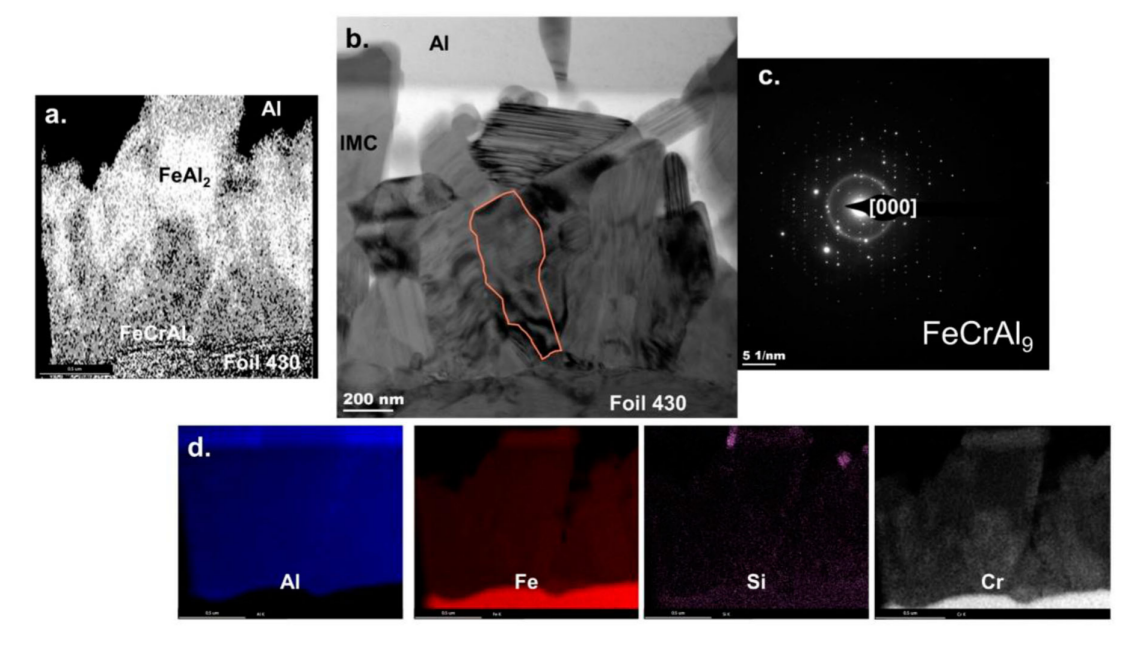


Figure 6. (a) Ratio of Fe and Crusing EDS maps from images in (d); (b) BF transmission electron microscope (TEM) images; (c) selected area diffraction (SAD) of highlighted grain; (d) TEM EDS mapping of the image in (a).

at.-%, less than what has been reported to inhibit the growth of the Fe–Al intermetallic [29–31]. FeAl₂ is a Fe-rich IMC that forms within a compositional range of 65 at.-% – 68 at.-%; thus, the high alloying of the PHS promoted the formation of FeAl₂. Consequently, as temperature increases Al atoms diffuse and interact with Fe atoms forming FeAl₂. Grain boundaries and dislocations are ideal sites for the nucleation and growth of intermetallic compounds because they lower the free energy of formation thus resulting in a defect-mediated mechanism [4]. In order to determine the effects of the

Cr on the intermetallic layer, the 430 foil condition was characterised since Ni was found not to affect the Fe–Al intermetallic.

Figure 6(a) shows a two-layer intermetallic comprising of, FeCrAl9 and FeAl2; FeAl3 was not observed. The thickness of the intermetallic layer was 1.1 $\mu m \pm 0.1$. Comparatively, the 304 foil intermetallic layer was 1.2 $\mu m \pm 0.1$ thick. The implementation of the stainless-steel interlayer reduced the thickness of the Fe–Al intermetallic by 0.7 μm . Figure 6(b) illustrates the formation of micro-twins within the intermetallic layer, which

can be linked to the segregation of Cr along the Fe-Al grain boundaries [32]. Figure 6(c) shows the diffraction pattern of the highlighted grain in Figure 6(b). ICSD reference 240189 was used to confirm the presence of a hexagonal FeCrAl₉ crystal within the Fe-Al layer. The crystal was viewed in the [001] orientation. EDS mapping (Figure 6(d)) shows the composition of FeCrAl₉ being 65.8 at.-% Al – 27.7 at.-% Fe – 6.5 at.-% Cr. FeAl₂ consisted of 68.5 at.-% Al – 29.4 at.-% Fe – 2.1 at.-% Cr. Cr segregation within the intermetallic layer is evident, as shown in Figure 6(d), resulting in the formation of FeCrAl9 and successfully suppressing the formation of FeAl₃. The change in composition along the Fe-Al layer through the segregation of Cr successfully inhibited the Fe-Al intermetallic, thus, resulting in secondary intermetallic phase formation.

Conclusions

In summary, dissimilar resistance spot welds were made using stainless-steel interlayers to inhibit the formation of the Fe-Al intermetallic. The thermodynamic simulations indicate a strong relationship between Cr and the Gibbs free energy of the FeAl₃ phase. A Cr wt-% of less than or equal to 25 wt-% is linearly correlated with temperature and found that at elevated temperatures where IMC growth is favoured, the Gibbs free energy of FeAl₃ is increased; thus, suppressing its formation and growth. The stainless-steel interlayers successfully mitigated the overall intermetallic layer thickness, with the 430 foil experiencing a 0.7 µm drop compared to the no interlayer thickness of 1.8 µm, which supported the kinetic simulation findings. The implementation of the stainless-steel interlayer was able to inhibit the Fe-Al intermetallic and improve joint performance under tensile shear loading conditions. The formation of FeCrAl₉ was discovered along the Fe-Al interface and FeAl₂. FeAl₃ did not form; therefore, the Fe-Al intermetallic growth can be successfully suppressed through Cr additions.

Acknowledgements

This work had support from Honda R&D Americas, Inc., Stellantis Metallic Materials Engineering R&D, and Arcelor-Mittal Global R&D. The authors would like to acknowledge the Manufacturing and Materials Joining Innovation Center (Ma2JIC), made possible through an award (1822144) from the National Science Foundation Industry-University Cooperative Research Center program (IUCRC), for financial and infrastructural support. Special thanks to Hendrik Colijn and the Center for Electron Microscopy and Analysis (CEMAS) at The Ohio State University for the SEM and TEM equipment used to perform the electron microscopy. The authors also thank colleagues Eric Brizes and Jacque Berkson, undergraduates Luke Kumler and Olivia Hupp of OSU welding engineering, Jim Rule and Benjamin Sutton of Thermo-Calc[©] for their helpful discussion on intermetallics. Also, thanks to Mark Fistler and Bill Trojanowski of Stellantis Metallic Materials Engineering R&D

Disclosure statement

No potential conflict of interest was reported by the author(s).

Funding

This work was supported by NSF [grant number 1822144].

ORCID

Antonio Ramirez http://orcid.org/0000-0002-4252-2857

References

- [1] Aydin H. Tensile Properties of Resistance Spot Welded Ultra High Strength Steel Usibor 1500 Optimization of electrical resistance spot welding parameters depending on microstructure and mechanical properties in TWIP sheets in different deformation ratios View project Oğuz Tunçel Siirt Üniversitesi; 2019.
- [2] Kleinbaum S, Jiang C, Logan S. Enabling sustainable transportation through joining of dissimilar lightweight materials. MRS Bull. Aug. 2019;44(8):608–612. doi:10. 1557/mrs.2019.178.
- [3] Zhang K, Bian X, Li Y, et al. New evidence for the formation and growth mechanism of the intermetallic phase formed at the Al/Fe interface. J Mater Res. 2013;28(23):3279–3287. doi:10.1557/jmr.2013.345.
- [4] Wan Z, Wang HP, Chen N, et al. Characterization of intermetallic compound at the interfaces of Al-steel resistance spot welds. J Mater Process Technol. Apr. 2017;242:12–23. doi:10.1016/j.jmatprotec.2016.11.017.
- [5] Oikawa H, Ohmiya S, Yoshimura T, et al. Resistance spot welding of steel and aluminium sheet using insert metal sheet. Sci Technol Weld Joining. 1999;4(2):80–88. doi:10.1179/136217199101537608.
- [6] Ibrahim I, Uematsu Y, Kakiuchi T, et al. Fatigue behaviour of dissimilar Al alloy / galvanised steel friction stir spot welds fabricated by scroll grooved tool without probe. Sci Technol Weld Joining. 2015;20(8): 670–679. doi:10.1179/1362171815Y.00000000053.
- [7] Sun YF, Fujii H, Takaki N, et al. Microstructure and mechanical properties of dissimilar Al alloy / steel joints prepared by a flat spot friction stir welding technique. Mater Des. 2013;47:350–357. doi:10.1016/j.matdes. 2012.12.007.
- [8] Chen C, et al. The robustness of Al-steel resistance spot welding process. J Manuf Process. Jul. 2019;43:300–310. doi:10.1016/j.jmapro.2019.02.030.
- [9] Zhang W, Sun D, Han L, et al. Characterization of intermetallic compounds in dissimilar material resistance spot welded joint of high strength steel and aluminum alloy; 2011.
- [10] Hu S, et al. Effect of external magnetic field on resistance spot welding of aluminium to steel. Sci Technol Weld Joining. 2022;27(2):84–91. doi:10.1080/13621718.2021. 2013707.
- [11] Zhang G, Zhao H, Xu X, et al. Metallic bump assisted resistance spot welding (MBaRSW) of AA6061-T6 and Bare DP590: Part II-joining mechanism and joint property. J Manuf Process. Aug. 2019;44:19–27. doi:10.1016/j.jmapro.2019.05.041.
- [12] Zhang W, Sun D, Han L, et al. Interfacial microstructure and mechanical property of resistance spot welded joint of high strength steel and aluminium alloy with 4047 AlSi12 interlayer. Mater Des. 2014;57:186–194. doi:10.1016/j.matdes.2013.12.045.



- [13] Winnicki M, Małachowska A, Korzeniowski M, et al. Aluminium to steel resistance spot welding with cold sprayed interlayer. Surf Eng. Mar. 2018;34(3):235-242. doi:10.1080/02670844.2016.1271579.
- [14] Lu Y, Mayton E, Song H, et al. Dissimilar metal joining of aluminum to steel by ultrasonic plus resistance spot welding - Microstructure and mechanical properties. Mater Des. Mar. 2019;165; doi:10.1016/j.matdes.2019. 107585.
- [15] Lara B, Giorjao R, Ramirez A. Resistance spot welding of printed interlayers to join Al-Fe sheets. Sci Technol Weld Joining. 2022. doi:10.1080/13621718.2022.210
- [16] Barmak K, Dybkov VI. Interaction of iron-chromium alloys containing 10 and 25 mass% chromium with liquid aluminium Part II formation of intermetallic compounds. J Mater Sci. Jul. 2004;39(13):4219-4230. doi:10.1023/B:JMSC.0000033402.37206.27.
- [17] Cheng WJ, Wang CJ. Effect of chromium on the formation of intermetallic phases in hot-dipped aluminide Cr-Mo steels. Appl Surf Sci. Jul. 2013;277:139-145. doi:10.1016/j.apsusc.2013.04.015.
- [18] Liu B, Yang Q, Wang Y. Intereaction and intermetallic phase formation between aluminum and stainless steel. Results Phys. 2019;12(Nov. 2018):514-524. doi:10.1016/j.rinp.2018.11.076.
- [19] Barmak K, Dybkov VI. Interaction of iron-chromium alloys containing 10 and 25 mass % chromium with liquid aluminium. J Mater Sci. 2003;38:3249-3255.
- [20] Cheng WJ, Wang CJ. Intermetallics effect of silicon on the formation of intermetallic phases in aluminide coating on mild steel. Intermetallics (Barking). Oct. 2011;19(10):1455-1460. doi:10.1016/j.intermet.2011.
- [21] Eggeler G, Auer W, Kaesche H. On the influence of silicon on the growth of the alloy layer during hot dip aluminizing. J Mater Sci. 1986;21(9):3348-3350. doi:10.1007/BF00553379.
- [22] Cheng WJ, Wang CJ. High-temperature oxidation behavior of hot-dipped aluminide mild steel with various silicon contents. Appl Surf Sci. Jun. 2013;274: 258-265. doi:10.1016/j.apsusc.2013.03.030.
- [23] Cheng WJ, Wang CJ. Microstructural evolution of intermetallic layer in hot-dipped aluminide mild steel

- with silicon addition. Surf Coat Technol. 2011;205(19): 4726–4731. doi:10.1016/j.surfcoat.2011.04.061.
- Chao YJ. Ultimate strength and failure mechanism of resistance spot weld subjected to tensile, shear, or combined tensile/shear loads. J Eng Mater Technol, Trans ASME. 2003;125(2):125-132. doi:10.1115/1.1555
- Brauser S, Pepke LA, Weber G, et al. Deformation [25] behaviour of spot-welded high strength steels for automotive applications. Mater Sci Eng A. 2010;527(26): 7099-7108. doi:10.1016/j.msea.2010.07.091.
- [26] Pouranvari M, Asgari HR, Mosavizadch SM, et al. Effect of weld nugget size on overload failure mode of resistance spot welds. Sci Technol Weld Joining. 2007;12(3):217-225. doi:10.1179/174329307X164409.
- [27] Shi L, Kang J, Shalchi Amirkhiz B, et al. Influence of sheet thickness ratio on fracture mechanisms of Al-steel resistance spot welds produced using multiring domed electrode. Sci Technol Weld Joining. Feb. 2020;25(2):164-168. doi:10.1080/13621718.2019. 1661115.
- [28] Scherf A, Kauffmann A, Kauffmann-Weiss S, et al. Orientation relationship of eutectoid FeAl and FeAl2. J Appl Crystallogr. 2016;49:442-449. doi:10.1107/S1600 576716000911.
- [29] Yin FC, Zhao MX, Liu YX, et al. Effect of Si on growth kinetics of intermetallic compounds during reaction between solid iron and molten aluminum. Trans Nonferrous Metals Soc China (English Edition). 2013;23(2):556-561. doi:10.1016/S1003-6326(13) 62499-1.
- [30] Yun JG, Lee JH, Kwak SY, et al. Study on the formation of reaction phase to Si addition in boron steel hot-dipped in Al-7Ni alloy. Coatings. 2017;7(11):1–16. doi:10.3390/coatings7110186.
- [31] Takata N, Nishimoto M, Kobayashi S, et al. Intermetallics morphology and formation of Fe e Al intermetallic layers on iron hot-dipped in Al e Mg e Si alloy melt. Intermetallics (Barking). 2014;54:136-142. doi:10.1016/j.intermet.2014.06.003.
- [32] Kovarik L, et al. Microtwinning and other shearing mechanisms at intermediate temperatures in Ni-based superalloys. Prog Mater Sci. Aug. 2009;54(6):839-873. doi:10.1016/j.pmatsci.2009.03.010.